J. Fluid Mech. (2015), *vol.* 779, *pp.* 776–793. © Cambridge University Press 2015
doi:10.1017/jfm.2015.456

Inertial migration of a spherical particle in laminar square channel flows from low to high Reynolds numbers

Naoto Nakagawa[1], Takuya Yabu[1], Ryoko Otomo[2], Atsushi Kase[1], Masato Makino[3], Tomoaki Itano[1] and Masako Sugihara-Seki[1,†]

[1]Department of Pure and Applied Physics, Kansai University, Suita, Osaka 564-8680, Japan

[2]Department of Mechanical Engineering, Kansai University, Suita, Osaka 564-8680, Japan

[3]Department of Mechanical Systems Engineering, Yamagata University, Yonezawa, Yamagata 992-8510, Japan

(Received 17 February 2015; revised 17 June 2015; accepted 31 July 2015; first published online 21 August 2015)

The lateral migration properties of a rigid spherical particle suspended in a pressure-driven flow through channels with square cross-sections were investigated numerically, in the range of Reynolds numbers (Re) from 20 to 1000. The flow field around the particle was computed by the immersed boundary method to calculate the lateral forces exerted on the particle and its trajectories, starting from various initial positions. The numerical simulation showed that eight equilibrium positions of the particle are present at the centres of the channel faces and near the corners of the channel cross-section. The equilibrium positions at the centres of the channel faces are always stable, whereas the equilibrium positions at the corners are unstable until Re exceeds a certain critical value, Re_c. At $Re \approx Re_c$, additional equilibrium positions appear on a heteroclinic orbit that joins the channel face and corner equilibrium positions, and the lateral forces along the heteroclinic orbit are very small. As Re increases, the channel face equilibrium positions are shifted towards the channel wall at first, and then shifted away from the channel wall. The channel corner equilibrium positions exhibit a monotonic shift towards the channel corner with increasing Re. Migration behaviours of the particle in the cross-section are also predicted for various values of Re. These numerical results account for the experimental observations of particle distributions in the cross-section of micro and millimetre scale channels, including the characteristic alignment and focusing of the particles, the absence of the corner equilibrium positions at low Re and the progressive shift of the equilibrium positions with Re.

Key words: multiphase and particle-laden flows, particle/fluid flow

1. Introduction

Inertial migration of suspended particles was first reported in Poiseuille flow through circular cylindrical tubes (Segre & Silberberg 1961). In dilute suspensions, neutrally buoyant spherical particles were observed to migrate across streamlines to

† Email address for correspondence: sekim@kansai-u.ac.jp

an equilibrium radial position. This phenomenon is due to the effect of inertia, as in the Stokes flow regime, a spherical particle translates parallel to the flow direction, regardless of its radial position, when it is rigid and neutrally buoyant. In recent years, this inertial focusing of suspended particles has attracted considerable attention in the field of microfluidics due to its broad range of applications, such as in the separation and filtration of particles and biological cells (e.g. Di Carlo 2009). For Reynolds numbers (Re) below approximately 100, experimental studies using microchannels with square cross-sections have shown the presence of four equilibrium positions for spherical particles centred at the faces of the channel (Di Carlo *et al.* 2007; Bhagat, Kuntaegowdanahalli & Papautsky 2008; Kim & Yoo 2008). Here, the Reynolds number is defined as $Re = UD/\nu$, where U is the average flow velocity, D is the width of the channel and ν is the kinematic viscosity of the fluid. The particle scale Reynolds number can be also defined as $Re_p = Re(d/D)^2$, where d denotes the diameter of suspended particles. Numerical simulations using a finite element method have supported the presence of channel face equilibrium positions for particles that are relatively large with respect to the width of the channel for $10 \leqslant Re \leqslant 40$ (Di Carlo *et al.* 2009), and this has been extended up to $Re = 120$ by a recent numerical study based on the force coupling method (Abbas *et al.* 2014). The locations of these equilibrium positions have been reported to move closer to the channel wall with increasing Re (Di Carlo *et al.* 2009; Choi, Seo & Lee 2011; Abbas *et al.* 2014), which is the same trend observed for circular cylindrical flows in experiments with a much wider range of Re up to 1700 (Segre & Silberberg 1962; Matas, Morris & Guazzelli 2004*a*,*b*) and in theoretical analyses based on the asymptotic theory valid for $Re_p \ll 1$ (Asmolov 1999; Matas, Morris & Guazzelli 2009).

In our recent study (Miura, Itano & Sugihara-Seki 2014), we performed experiments on the inertial migration of neutrally buoyant spherical particles immersed in square channel flows in Re ranges from 100 to 1200. Observations of the particle distribution in several cross-sections of the channel indicated that four equilibrium positions at the centres of the channel faces are also present in this Re range, and an additional equilibrium position appears near each channel corner for Re greater than a certain critical value, Re_c (≈ 260). The former equilibrium positions were termed the channel face equilibrium positions, while the latter were termed the channel corner equilibrium positions. It was shown that the channel corner equilibrium positions move away from the channel centre and the channel face equilibrium positions approach the channel centre as Re increases.

Chun & Ladd (2006) conducted a numerical study of the motion of spherical particles suspended in square channel flows utilizing the lattice-Boltzmann method at Reynolds numbers between 100 and 1000. Although some of their results were consistent with the experimental observations of Miura *et al.* (2014), there were also some striking differences between them. Chun & Ladd (2006) predicted that several equilibrium positions are present, including the corner equilibrium positions, at $Re = 100$, while for Re larger than 500, only corner equilibrium positions exist. This is contradictory to the experimental observations of Miura *et al.* (2014) described above. In addition, they predicted an outward shift of the equilibrium positions toward the channel wall with increasing Re, although Miura *et al.* (2014) observed an inward shift of the channel face equilibrium positions for Re larger than about 200.

In the present study, we utilize an immersed boundary method to perform a numerical simulation of the motion of a neutrally buoyant spherical particle suspended in the square channel flows corresponding to the experiments of Miura *et al.* (2014). The Reynolds numbers investigated here range from 20 to 1000, which also covers

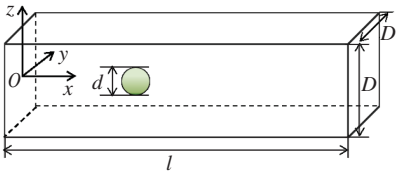

FIGURE 1. (Colour online) Configuration for a neutrally buoyant spherical particle of diameter d suspended in a pressure-driven flow through a square channel of width D. The computational domain has length l in the undisturbed flow direction, at both ends of which we apply periodic boundary conditions.

experiments using microchannels. We have focused on large particles, with a diameter of about 1/10 of the channel width, which is a representative size ratio for previous studies on inertial migration. The numerical simulation presented here successfully describes the experimental results for both micro scale and larger millimetre scale channel flows. For Re smaller than about 260, only channel face equilibrium positions are present, whereas for Re beyond this value, additional equilibrium positions appear near the channel corners. An increase in Re from small values is predicted to produce an outward shift of the channel face equilibrium positions in the range of Re for microchannel flows, followed by the inward shift in the range of Re for millimetre scale channel flows. In addition, the migration behaviours of the particles in the channel cross-section are also predicted, which account for the particle distributions observed experimentally at several cross-sections downstream of the channel inlet.

2. Numerical method

We consider the motion of a single spherical particle immersed in a pressure-driven flow of an incompressible Newtonian fluid through a square channel, as shown in figure 1. The x-axis is taken along the centreline of a square channel of width D. The channel walls are located at $y = \pm D/2$ and $z = \pm D/2$. The particle of diameter d is assumed to be neutrally buoyant, i.e. the densities of the fluid and the particle are equal.

The governing equations for the fluid flow are the equation of continuity and the Navier–Stokes equations. The motion of the suspended particle obeys Newton's second law of motion. These equations are solved numerically using the immersed boundary method proposed by Kajishima *et al.* (2001). Briefly, we introduce the average velocity of the fluid and the particle in terms of a scalar, α,

$$\boldsymbol{u} = (1-\alpha)\boldsymbol{u}_f + \alpha \boldsymbol{u}_p, \tag{2.1}$$

where $\boldsymbol{u}_f$ represents the fluid velocity and $\boldsymbol{u}_p$ represents the velocity inside the particle, which satisfies

$$\boldsymbol{u}_p = \boldsymbol{V} + \boldsymbol{\Omega} \times \boldsymbol{R}. \tag{2.2}$$

Here, $\boldsymbol{V}$ is the translational velocity, $\boldsymbol{\Omega}$ is the angular velocity of the particle relative to the particle centre, and $\boldsymbol{R}$ is the position vector from the particle centre. The scalar α represents the volume fraction of the solid phase (particle) occupying the computational cell considered; $\alpha = 0$ in the fluid region and $\alpha = 1$ inside the particle. Thus, the velocity $\boldsymbol{u}$ in (2.1) represents the volume-weighted velocity average in each computational cell.

For the no-slip condition at the surface of the particle, it can be shown that the average velocity $\boldsymbol{u}$ satisfies the equation of continuity:

$$\nabla \cdot \boldsymbol{u} = 0. \tag{2.3}$$

Corresponding to the Navier–Stokes equations for $\boldsymbol{u}_f$, we use the following equation for $\boldsymbol{u}$:

$$\rho \left\{ \frac{\partial \boldsymbol{u}}{\partial t} + (\boldsymbol{u} \cdot \nabla)\boldsymbol{u} \right\} = -\nabla p + \mu \nabla \cdot [\nabla \boldsymbol{u} + (\nabla \boldsymbol{u})^{\mathrm{T}}] + \boldsymbol{f}, \tag{2.4}$$

where p is the pressure, ρ is the density and μ is the viscosity of the fluid. The force term on the right-hand side of equation (2.4), $\boldsymbol{f}$, represents the interaction between the fluid and solid phases, and is determined such that it satisfies the condition that the velocity inside the particle coincides with the particle velocity (2.2). The value of $\boldsymbol{f}$ is evaluated at each time step in the time-marching procedure using a fractional step method (Kajishima *et al.* 2001). For boundary conditions, we adopt the no-slip condition at the channel walls at $y = \pm D/2$ and $z = \pm D/2$, and periodic conditions at the upstream and downstream ends of the channel at $x = 0$ and l. A constant pressure difference is also applied between both ends.

As $\boldsymbol{f}$ represents the force exerted on the fluid by the particle, $-\boldsymbol{f}$ acts on the particle. Thus, the motion of the particle can be determined by

$$\frac{\mathrm{d}(m\boldsymbol{V})}{\mathrm{d}t} = -\int_V \boldsymbol{f}\,\mathrm{d}V, \quad \frac{\mathrm{d}(\boldsymbol{I} \cdot \boldsymbol{\Omega})}{\mathrm{d}t} = -\int_V \boldsymbol{r} \times \boldsymbol{f}\,\mathrm{d}V, \tag{2.5a,b}$$

where m and $\boldsymbol{I}$ represent the mass and moment of inertia of the particle, respectively. The integrations are performed over the volume of the particle.

Equations (2.5) are used to calculate the trajectories of a particle that is floating freely in the flow. To calculate the lateral forces F_y and F_z exerted on the particle by the fluid flow, we assume that the suspended particle moves freely in the x-direction and rotates freely in all directions, but does not move laterally. In this case, we use the following equations instead of equations (2.5):

$$\frac{\mathrm{d}(mV_x)}{\mathrm{d}t} = -\int_V f_x\,\mathrm{d}V, \quad \frac{\mathrm{d}(\boldsymbol{I} \cdot \boldsymbol{\Omega})}{\mathrm{d}t} = -\int_V \boldsymbol{r} \times \boldsymbol{f}\,\mathrm{d}V, \tag{2.6a,b}$$

together with the condition of $V_y = V_z = 0$, and calculate the lateral force (F_y, F_z) by

$$F_y = -\int_V f_y\,\mathrm{d}V, \quad F_z = -\int_V f_z\,\mathrm{d}V. \tag{2.7a,b}$$

To determine the value of α, Kajishima *et al.* (2001) evaluated the volume fraction of the solid phase in the computational cell by approximating the particle surface by a plane tangential to it. In the present study, we adopt for each computational cell

$$\alpha = \frac{1}{2}\left\{ 1 - \tanh \frac{|\boldsymbol{R}| - d/2}{\xi} \right\}, \tag{2.8}$$

where $\boldsymbol{R}$ is the position vector of the centre of the computational cell relative to the particle centre and ξ represents the width of the interface between the fluid and the particle, which is chosen to be comparable to the width of the computational cell, Δ (Nakayama & Yamamoto 2005).

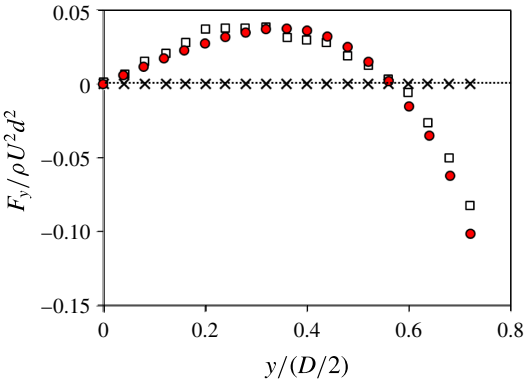

FIGURE 2. (Colour online) Non-dimensional lateral forces F_y (filled circles) and F_z (crosses) exerted on a particle when the particle is placed on the y-axis for $d/D = 0.22$ and $Re = 40$. The corresponding results for F_y obtained by Di Carlo *et al.* (2009) are shown by hollow squares.

The numerical scheme was validated and the accuracy was assessed in two cases. In the first case, we computed the drag force acting on a stationary spherical particle in an unbounded uniform flow and compared the obtained results with the reference (Bird, Stewart & Lightfoot 2007), in the same manner as Kajishima *et al.* (2001) tested the numerical method in a wide range of the Reynolds number Ud/ν for various spacial resolutions Δ. Here, U represents the velocity of the uniform flow. Similar to the estimate of Kajishima *et al.* (2001), the present simulation yielded about 8 % error in the drag force for $\Delta/d = 0.1$ and at most 5 % error for $\Delta/d = 0.05$ at $Ud/\nu \leqslant 200$, corresponding to $Re = UD/\nu \leqslant 1800$ for $d/D = 0.11$. In order to treat a turbulent flow of multiparticle suspensions, they adopted $\Delta/d = 0.125$, which provided less than 10 % error in the drag force for $Ud/\nu \leqslant 400$. In the present study, we set $\Delta/d = 0.05$.

In the second case, the results of the present problem were compared with previous studies for low Reynolds numbers. Di Carlo *et al.* (2009) treated a similar problem with a finite element method for a relatively large particle for $Re \leqslant 40$. We performed a computation using their parameter values and compared the results, as shown in figure 2. This shows the lateral force F_y exerted on a particle placed at various positions on the y-axis with $d/D = 0.22$ and $Re = 40$. Although fairly good agreement was obtained overall, there were some discrepancies, especially for a particle placed close to the channel walls. The relative error between the two results was about 10 % on average. One reason for these discrepancies may be that the precise results of Di Carlo *et al.* (2009) were difficult to read from figure 3 of their paper. The present computation confirmed that the lateral forces F_z vanish at all positions (crosses in figure 2), as expected from symmetry considerations. The intersection of the force curve F_y with the horizontal axis in figure 2 indicates the location of an equilibrium position where the resultant lateral force vanishes. The channel face equilibrium positions thus obtained showed good agreement between the present results and the corresponding results in figure 3 of Di Carlo *et al.* (2009) within about 2 % error for $d/D = 0.22$ and 0.30 at $Re = 40$. Further comparisons of the present results with other previous studies can be seen in figure 8(*a*).

The effect of the channel length l on the computational results was examined for various Reynolds numbers in the case of $d/D = 0.11$. The lateral forces computed at several positions in the cross-section for $l/d = 10$, 20, and 30 were compared with the

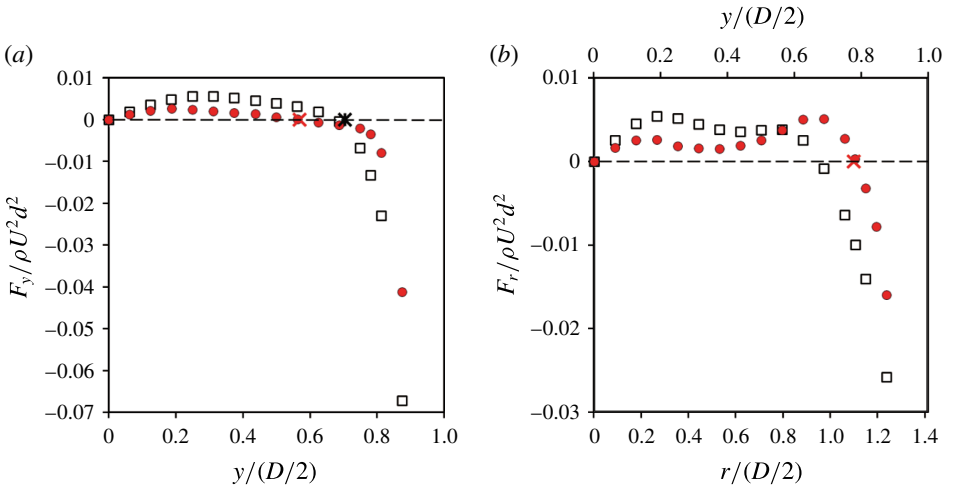

FIGURE 3. (Colour online) (*a*) Non-dimensional lateral force F_y when the particle is placed on the y-axis, and (*b*) non-dimensional lateral force F_r along the diagonal when the particle is placed on the diagonal. The variable r represents the distance from the channel centre. The hollow squares represent the values at $Re = 144$ and the filled circles correspond to $Re = 514$. The asterisk and the cross correspond to the experimental results at $Re = 144$ and $Re = 514$, respectively (Miura *et al.* 2014).

corresponding values for $l/d = 50$. The differences between the values for $l/d = 10$ and 50 varied depending on the positions, but the differences between $l/d = 20$ or 30 and 50 were less than 2 % at $Re = 514$ and about 3 % at $Re = 968$. In addition, the locations of the equilibrium position determined from the lateral force profiles showed a good agreement between the cases of $l/d = 20$ and 50. Thus, we adopted $l/d = 20$ in the present study.

In the experiments of Miura *et al.* (2014), the distributions of the particle centres were observed at downstream cross-sections of square channels of width $D = 6.0$ mm for neutrally buoyant spherical particles of diameter $d = 0.65$ mm. Corresponding to these experiments, we report here cases for $d/D = 0.11$. This size ratio is comparable with previous experimental and numerical studies, including Chun & Ladd (2006) ($d/D = 0.11$), Di Carlo *et al.* (2007) (0.18), Bhagat *et al.* (2008) (0.07–0.1), Choi *et al.* (2011) (0.075–0.16) and Abbas *et al.* (2014) (0.11). In computing the trajectories of the particle, we adopted an undisturbed fluid velocity and half of the undisturbed vorticity vector at the centre of the particle as the initial conditions for $\boldsymbol{V}$ and $\boldsymbol{\Omega}$, respectively. The lateral forces (F_y, F_z) were estimated after the particle reached a steady state.

3. Results and discussion

3.1. *Lateral forces at low and high Reynolds numbers*

As representative examples, the lateral forces exerted on a particle are plotted in figure 3(*a*,*b*) when the particle is placed on the y-axis or on the diagonal, respectively, for $Re = 144$ and 514. In figure 3(*b*), r ($= \sqrt{y^2 + z^2}$) represents the distance from the channel centre and F_r denotes the lateral force along the diagonal. In both figures, the outward forces toward the channel walls act on the particle when it is

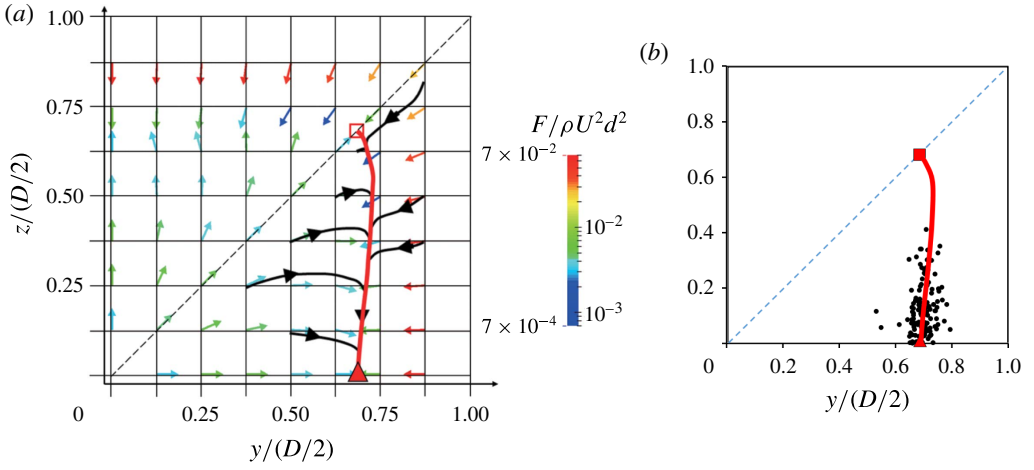

FIGURE 4. (*a*) Map of the lateral forces (F_y, F_z) and trajectories of the particle centre projected over the channel cross-section at $Re = 144$. Each arrow at the lattice represents the direction of the lateral force, and its magnitude is indicated by the colour. The triangle represents the channel face equilibrium position, which is stable, and the square shows the channel corner equilibrium position, which is unstable. The thick red line represents the heteroclinic orbit that joins the channel face equilibrium position and the corner equilibrium position. (*b*) Particle distribution obtained experimentally at $Re = 144$. (Miura *et al.* 2014) and the heteroclinic orbit obtained numerically. Each dot represents the location of a particle centre observed in the cross-section.

located close to the channel centre, whereas significant wall repulsion forces act on the particle when it is placed near the channel walls. In all cases computed, one equilibrium position exists at a location between the channel centre and the channel wall, which is determined as the intersection of the force curve with the horizontal axis. The intersection on the y-axis, shown in figure 3(*a*), represents the channel face equilibrium position, and the intersection on the diagonal, shown in figure 3(*b*), represents the channel corner equilibrium position.

Miura *et al.* (2014, 2015) observed the distributions of particle centres at downstream channel cross-sections, and determined the locations of equilibrium positions as local maximum positions of the probability density function of the particles. At $Re = 144$, the equilibrium positions thus determined are present only at the centre of the channel faces, while at $Re = 514$, both the channel face and channel corner equilibrium positions are present. In figure 3(*a*,*b*), experimentally obtained equilibrium positions are indicated by an asterisk for $Re = 144$ and a cross for $Re = 514$, respectively. The locations of these equilibrium positions showed excellent agreement with the present numerical results, although there are some deviations in the experimental measurements (see figure 8*a*,*b*). At $Re = 144$, the present numerical simulation predicts the presence of channel corner equilibrium positions, whereas they are not observed experimentally. We think that the channel corner equilibrium positions are unstable for Re smaller than a certain critical value, Re_c, and so they cannot be observed experimentally for $Re < Re_c$. This is discussed below.

Figure 4(*a*,*b*) show a map of the lateral forces (F_y, F_z) in the first quadrant of the channel cross-section at $Re = 144$ ($< Re_c$), and the corresponding experimental particle distribution results (Miura *et al.* 2014). In figure 4(*a*), each arrow represents

the direction of the lateral force acting on a particle located at the origin of the arrow, with the magnitude expressed by the colour. Several representative trajectories of the particle centre projected over the cross-section are also plotted with black lines. In figure 4(*b*), each dot represents the location of a particle centre observed in the cross-section; the data are summed over the region of the azimuthal angle between 0 and $\pi/4$ based on symmetry considerations.

In figure 4(*a*), the red square represents the channel corner equilibrium position on the diagonal, the location of which is determined from the force curve shown in figure 3(*b*). Trajectories starting from the neighbourhood of the corner equilibrium position lead away from this location, indicating that the corner equilibrium position is unstable. In addition, trajectories starting from various initial positions approach the channel face equilibrium position (red triangle in figure 4*a*), indicating that the channel face equilibrium position is stable. This is the reason why no particles are observed near the channel corners and most particles are placed near the centre of the channel face in figure 4(*b*).

From the trajectories illustrated in figure 4(*a*), we notice that the particles migrate in two stages. In the first stage, they move in nearly radial directions until they reach a single line that represents a heteroclinic orbit joining the channel face equilibrium position and the corner equilibrium position (red line in figure 4*a*). In the second stage, the particles travel along the heteroclinic orbit toward the channel face equilibrium position. In accordance with this prediction, figure 4(*b*) shows that the particles observed experimentally are almost aligned along the heteroclinic orbit, with most particles focused near the channel face equilibrium position. The first stage is a relatively fast process, while the second stage is slower. We will show in § 3.3 that the time scale, or the travelling distance in the flow direction during each stage, depends on not only the particle position but also the Reynolds number.

The present results shown in figure 4(*a*) at $Re = 144$ are consistent with previous studies for microchannel flows for $1 \leqslant Re \leqslant 120$. For the same size ratio with the present study ($d/D = 0.11$), Abbas *et al.* (2014) made microscope measurements of particles suspended in square microchannel flows and numerical analyses of the trajectories of a single particle based on the force coupling method. The trajectories at $Re = 120$ shown in figure 8 of their paper are comparable to those shown in figure 4(*a*), although the locations of the channel face equilibrium positions obtained in the present study are closer to their experimental results rather than their numerical results (see our figure 8*a*).

At lower Re ($= 40$) and for larger particles ($d/D = 0.22$), the distribution of the lateral forces in the cross-section was calculated by a finite element computation (Di Carlo *et al.* 2009) and by a perturbation analysis (Hood, Lee & Roper 2015). While not shown here, we have also plotted the map of the lateral forces and computed the trajectories for $Re = 50$ and $d/D = 0.11$ (Nakagawa *et al.* 2014), which were found to have similar features to figure 4(*a*); outward forces are exerted on the particle in the inner region of the heteroclinic orbit, whereas in the outer region significant repulsion forces act, with the magnitude being larger nearer to the centre of the channel face and weaker nearer to the corner. There is also a stable equilibrium position at the centre of each channel face, and an unstable equilibrium position at each corner. These features are also observed in figure 1 of Di Carlo *et al.* (2009), despite the difference in size ratio d/D. Hood *et al.* (2015) estimated the lateral forces using a regular perturbation method from the Stokes flow regime. Although the trajectories and the lateral force distribution shown in figure 8 of their paper are qualitatively similar to the present results, there seem some discrepancies in the region near the channel wall and

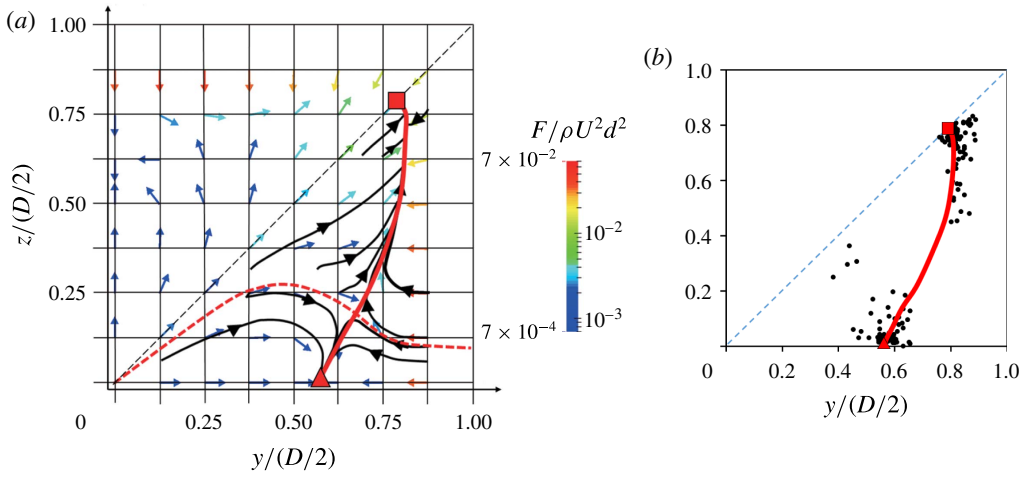

FIGURE 5. (*a*) Map of the lateral forces (F_y, F_z) and trajectories of the particle centre projected over the channel cross-section at $Re = 514$. At this Re, both the channel face equilibrium position (triangle) and the channel corner equilibrium position (square) are stable. The thick red solid line represents the heteroclinic orbit and the thick red dashed line represents the separatrix. (*b*) Particle distribution obtained experimentally at $Re = 514$ (Miura *et al.* 2015) and the heteroclinic orbit obtained numerically. For additional explanation, see figure 4.

around the channel corner equilibrium positions; the lateral forces in that region are rather weak compared to Di Carlo *et al.* (2009) and the present study. Large repulsion forces on the particles near the channel wall were reported experimentally by Choi *et al.* (2011) in the range of $2.4 \leqslant Re \leqslant 60$. Since the effect of the channel wall was calculated by the method of reflections in Hood *et al.* (2015), a finite number of reflections may lead to the rather weak repulsion force when a large particle is placed close to the channel wall.

The map of the lateral forces computed at $Re = 514\ (> Re_c)$ and the corresponding experimental results of the particle distribution (Miura *et al.* 2015) are shown in figure 5(*a*,*b*), respectively. Several trajectories of the particle centre are plotted with black lines in figure 5(*a*). The trajectories indicate that at this Reynolds number, both the channel face and channel corner equilibrium positions are stable, and separatrix (red dashed line) as well as a heteroclinic orbit (red solid line) appear in figure 5(*a*). The intersection of these two lines represents a saddle point. The trajectories in figure 5(*a*) also suggest a two stage migration of the particles: migration up to the heteroclinic orbit in the first stage and migration along the heteroclinic orbit toward either the channel face or corner equilibrium position in the second stage. This property is exemplified in figure 5(*b*), which shows the alignments of particles along the heteroclinic orbit near the channel face and channel corner equilibrium positions.

To the authors' knowledge, there are no comparable studies investigating the lateral forces on a particle suspended in square channel flows at this Re, except Chun & Ladd (2006). They reported from their numerical simulation, using the lattice Boltzmann method, that only the channel corner equilibrium positions are stable and the channel face equilibrium positions are unstable above $Re = 500$. This result does not match our experiments (Miura *et al.* 2014, 2015) and the present numerical simulation shown in figure 5(*a*). For low Re (≈ 100), Chun & Ladd (2006) found stable equilibrium

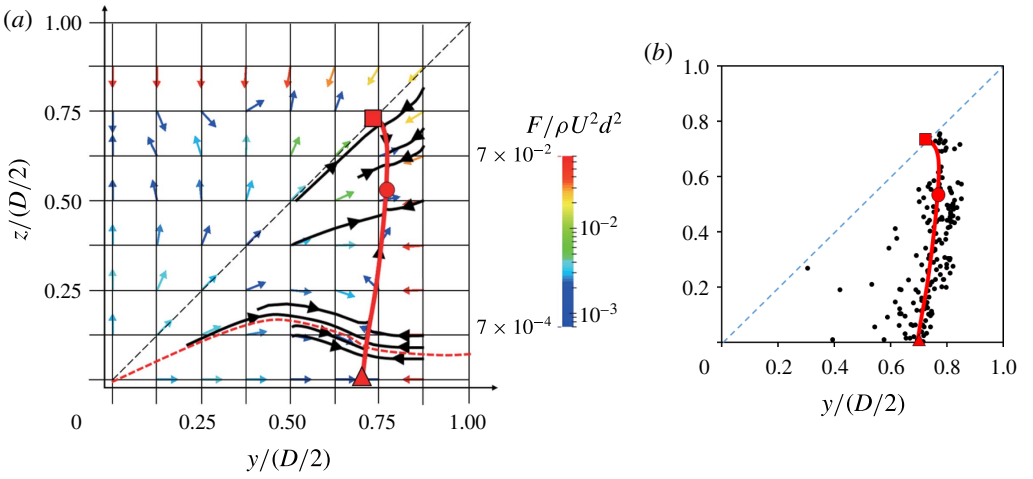

FIGURE 6. (*a*) Map of the lateral forces (F_y, F_z) and trajectories of the particle centre projected over the channel cross-section at $Re = 260$. At this Re, an additional stable equilibrium position (red circle) appears on the heteroclinic orbit (thick red solid line). (*b*) Particle distributions obtained experimentally at $Re = 260$ (Miura *et al.* 2014) and the heteroclinic orbit obtained numerically. For additional explanation, see figure 4.

positions in corners and faces while in the following numerical studies (Di Carlo *et al.* 2009; Abbas *et al.* 2014), including the present study, and in experimental studies (Kim & Yoo 2008; Di Carlo *et al.* 2009; Choi *et al.* 2011; Abbas *et al.* 2014; Miura *et al.* 2014), the corner corner equilibrium positions were indicated to be unstable. With regard to the discrepancy at low Re ($\approx$ 100), Abbas *et al.* (2014) reported from their numerical simulations, adopting a very short computational domain, that the particle can be pushed towards the channel corner instead of the centre of the channel face at $Re = 120$, suggesting that the inter-particle interaction in the flow direction may result in the presence of the channel corner equilibrium position at low Re. Chun & Ladd (2006) employed a periodic channel length of $l/d = 5$ for their simulations at $Re = 100$–1000. Thus, the discrepancy observed at high Re ($\approx$ 500) may also originate from the hydrodynamic interaction between particles, since the wake of a particle could be larger and longer as Re increases. We will examine the effect of the channel length on the particle behaviour at high Re in a future study.

3.2. *Lateral forces near the critical Reynolds number*

The present numerical study showed that both the channel face and channel corner equilibrium positions always exist in the range of Re computed, but in fact the channel corner equilibrium positions are unstable until the Reynolds number exceeds a certain critical value, Re_c (≈ 260). Figure 6(*a*,*b*) show a map of the lateral forces computed at $Re = 260$ and the corresponding experimental particle distribution (Miura *et al.* 2014), respectively. Near this Re, it was shown experimentally that additional equilibrium positions appear at azimuthal angles of $\sim$0.5–0.7 rad, as well as the channel face equilibrium positions (Miura *et al.* 2014, 2015). Corresponding to this observation, the present computation showed the presence of another stable equilibrium position on the heteroclinic orbit at $Re = 260$, which is indicated by a

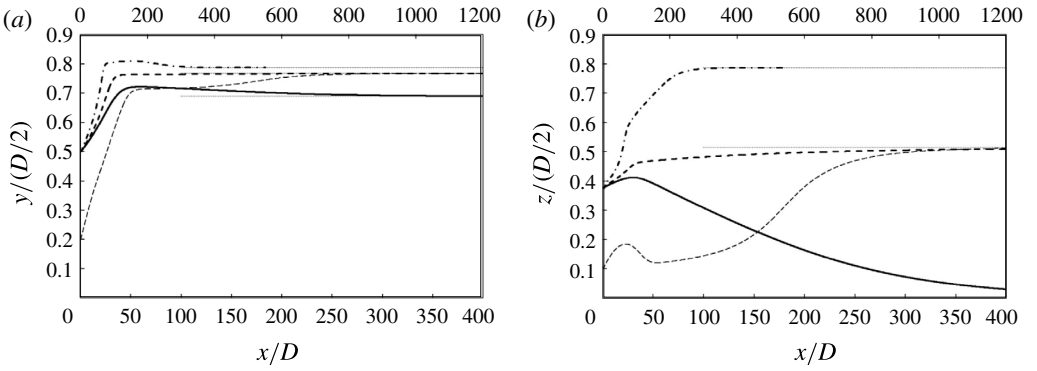

FIGURE 7. Particle trajectories in (*a*) the (*x*, *y*) plane and (*b*) the (*x*, *z*) plane, starting from $(y/(D/2), z/(D/2)) = (0.5, 0.375)$, at $Re = 144$ (solid line), 260 (dashed line) and 514 (dash-dotted line). The horizontal dotted lines denote the asymptotic coordinates the trajectories approach. The dashed thin lines represent the trajectories, starting from $(y/(D/2), z/(D/2)) = (0.2, 0.1)$, at $Re = 260$. Note that the *x*-scale for this case is shown on the upper horizontal axis.

red circle in figure 6(*a*). This location, of azimuthal angle 0.59 rad, is close to the equilibrium position observed experimentally. One of the characteristics at this Re is that the magnitudes of the lateral forces are very small along the heteroclinic orbit. This property may be demonstrated in figure 6(*a*), in which the trajectories (black lines) enter the heteroclinic orbit (red line) at almost right angles. The particles in the second stage move very slowly along the heteroclinic orbit, taking a long time to reach the stable equilibrium position (see figure 7). The magnitudes of the lateral forces are so small that other equilibrium positions may be present on the orbit. The slow movement in the second stage may be reflected in the experimental observation that the particles shown in figure 6(*b*) are aligned along almost entire circumference of the heteroclinic orbit and the focusing near the equilibrium positions is weak.

In order to examine the stability of the channel corner equilibrium position from the lateral force profile, we computed the azimuthal component of the lateral force, F_θ, along a short circular arc passing the corner equilibrium position at $Re = 144$, 260 and 514. The computations in the range of θ from $\pi/4$ to $\pi/4 - 0.025$ rad indicated that, as θ decreases from $\pi/4$, F_θ decreases monotonically from zero at $Re = 144$, whereas F_θ increases monotonically from zero at $Re = 514$. Since the radial component of the lateral force, F_r, vanishes at the corner equilibrium position, varying from positive to negative values with r along the diagonal, this result implies that the corner equilibrium position is a saddle point at $Re = 144$ and it is a stable equilibrium point at $Re = 514$. The magnitudes of $F_\theta/\rho U^2 d^2$ at $\theta = \pi/4 - 0.025$ rad are about 2×10^{-4} at $Re = 144$ and 514. On the other hand, at $Re = 260$ the maximum value of $F_\theta/\rho U^2 d^2$ in this range of θ is about one-tenth of this value, i.e. F_θ is extremely small, indicating that this Reynolds number is close to the critical value, Re_c. The similar computations at $Re = 300$ also yielded small values of F_θ in the same range of θ. As such subtle variations in the lateral forces may be beyond the accuracy of the current numerical method, further analyses of higher precision are necessary to determine the critical Reynolds number.

3.3. *Entry length for focusing*

The trajectories shown in figures 4(*a*)–6(*a*) clearly demonstrate the two stage properties of the particle migration. As a representative example of the particle behaviour at each Re, the projections of the trajectories onto the (x, y) and (x, z) planes, starting from $(y/(D/2), z/(D/2)) = (0.5, 0.375)$ in the cross-section, are plotted at $Re = 144$, 260 and 514 in figure 7. The horizontal dotted lines represent the coordinates of the asymptotic position where the trajectory approaches: the channel face equilibrium position at $Re = 144$ (triangle in figure 4*a*), the stable equilibrium position on the heteroclinic orbit at $Re = 260$ (circle in figure 6*a*) and the channel corner equilibrium position at $Re = 514$ (square in figure 5*a*). The first stage continues until the particle reaches the heteroclinic orbit. The travelling distance in the flow direction during the first stage can be estimated from figure 7 as $L_1/D \approx 50$, 35 and 30 at $Re = 144$, 260 and 514, respectively. The value of $L_1/D \approx 50$ at $Re = 144$ agrees with the result for $Re = 120$ reported by a numerical simulation of Abbas *et al.* (2014), although the initial position of the trajectory is different.

After the first stage, the particle translates much slower along the heteroclinic orbit towards the stable equilibrium position in the second stage. Figure 7 shows that the second stage continues until the travelling distance $L_2/D \approx 600$ and 100 from the channel inlet, at $Re = 144$ and 514, respectively, indicating that L_2 is about ten times and several times larger than L_1 at $Re = 144$ and 514, respectively. These values of L_2 were estimated from the axial distance where the centre of particle approaches within $0.005 \times (D/2)$ to the asymptotic position. The value of $L_2/D \approx 600$ at $Re = 144$ is about a half of the result of Abbas *et al.* (2014) for $Re = 120$, which is presumably due to the difference in the initial position as well as the Reynolds number, or the method of estimate for L_2. They reported that $L_2/D \approx 1000$ at both $Re = 60$ and 120, and figure 9 of their paper showed that, at $Re = 12$, the particle did not approach within a close distance to the asymptotic position even at $x/D = 3000$, indicating that $L_2/D > 3000$ at $Re = 12$. The present study indicated that the axial distance of the second stage is, in general, longer for smaller Re, which seems consistent with the results of Abbas *et al.* (2014).

Near the critical Reynolds number, however, the lateral velocity of the particle moving along the heteroclinic orbit is so small that the particle keeps migrating in much longer axial distance in the second stage, as seen from the curve for $Re = 260$ in figure 7. As another example for this Reynolds number, a trajectory starting from $(y/(D/2), z/(D/2)) = (0.2, 0.1)$ is also plotted by thin dashed lines in figure 7(*a*,*b*). Note that the horizontal axis for these curves is shrunk by one-third (the scale is shown on the upper axis). In this case also, the particle approaches asymptotically the stable equilibrium position on the heteroclinic orbit (circle in figure 6*a*). The travelling distance before reaching the stable equilibrium position is estimated to be $L_2/D \approx 1100$ from figure 7. Thus, it is demonstrated that, at $Re \approx Re_c$, L_2 is much larger than L_1, possibly by two orders of magnitude. Therefore, we conclude from the present results that an increase in Re decreases L_1 and it also decreases L_2 in general, but for $Re \approx Re_c$, L_2 could be extremely large compared to L_1.

In Miura *et al.* (2014), we have discussed the entry length after which lateral migration has fully developed. Assuming that the lateral force is balanced by a viscous Stokes drag, we derived the conventional expression of the entry length L_e as $L_e/l' \approx 6\pi A^{-1} Re^{-1} (d/D)^{-3}$ (Matas *et al.* 2004*a*; Di Carlo *et al.* 2007) when the lateral force is expressed as $F = A(d/D)^4 \rho U^2 D^2$, which was suggested from an asymptotic theory (Ho & Leal 1974; Schonberg & Hinch 1989). Here, l' represents a lateral migration distance and A is a constant, depending on the particle position in the

cross-section as well as the Reynolds number. Although an alternative expression of L_e/l' proportional to $(d/D)^{-2}$ instead of $(d/D)^{-3}$ may be obtained for microchannel flows (Di Carlo 2009; Choi *et al.* 2011), there are no differences between these two expressions in the case of a fixed size ratio d/D as in the present study. Considering the two stage migration properties, we notice that the entry length L_e estimated from the above formula may correspond to the length of the first stage, L_1. Thus, we here estimate the entry length L_e using the magnitude of the lateral force obtained in the present numerical computations and compare them with the values of L_1 obtained from the trajectories shown in figure 7.

Figures 4(*a*)–6(*a*) indicate that $F/\rho U^2 d^2 \approx 4$, 3 and 2×10^{-3} at $Re = 144$, 260 and 514, respectively, in the region near $(y/(D/2), z/(D/2)) = (0.5, 0.375)$. These values lead to $L_e/D \approx 50$, 36 and 28 at $Re = 144$, 260 and 514, respectively, if we assume $l' \approx D/6$, i.e. the lateral migration distance is set to be one-sixth of the channel width in the first stage. These estimates show good agreement with the above values of L_1 obtained for thick lines in figure 7. Thus, L_e is indicated to provide the length of the first stage L_1. It may be useful to note that the entry length L_e, in general, decreases slower than Re^{-1} with increasing Re, since an increase in Re decreases the constant A in the force expression, as shown in the present study.

The main findings of the present study include that the length of the second stage, L_2, is much larger than L_1 or L_e. This result suggests that the length of channels required for particle focusing is much larger than L_e, which rationalizes the experimental observation of Miura *et al.* (2014); the entry length L_e estimated using the above formula was much shorter than that expected from the experimental results of the particle distribution. For microchannel flows at low Re ($\leqslant 60$), the experimental study of Choi *et al.* (2011) reported that the focusing on the channel face equilibrium position was rather weak in the second stage when the particle distributions were measured at $240D$–$950D$ downstream of the entrance. When the measurements were performed at $640D$ downstream, the fractions of the particles located in the region of $-5^\circ \leqslant \theta \leqslant 5^\circ$ around the channel face equilibrium position were less than 30 % for $d/D = 0.075$ and about 50 % for $d/D = 0.16$, at $Re = 60$. For smaller Re, the fractions were reduced even when the measurements were performed further downstream. In their study, the length of L_e estimated using the above formula described well their experimental observation for the first stage, and L_2 was assessed to be twice of this length. However, these weak focusing properties in the second stage may imply longer L_2 than that of the authors' assessment in their paper. Further studies may be required for the entry length, since this information is one of the most important factors for the design of microchannels for practical applications such as separation, filtration and sorting of particles. We will return to this matter again at the end of the next section.

3.4. *Reynolds number dependence of the equilibrium positions*

The locations of the channel face and corner equilibrium positions, y_e, are plotted against Re in figure 8(*a*,*b*), together with the experimental data (Miura *et al.* 2014, 2015). In figure 8(*a*), the results of microchannel experiments at lower Re are also plotted for comparable size ratios ($d/D = 0.075$–0.17). The present numerical simulation showed that the channel face equilibrium positions always exist in the range of Re from 20 to 1000 and they are stable. As Re increases from small values, micro scale experiments have demonstrated an initial increase in equilibrium position

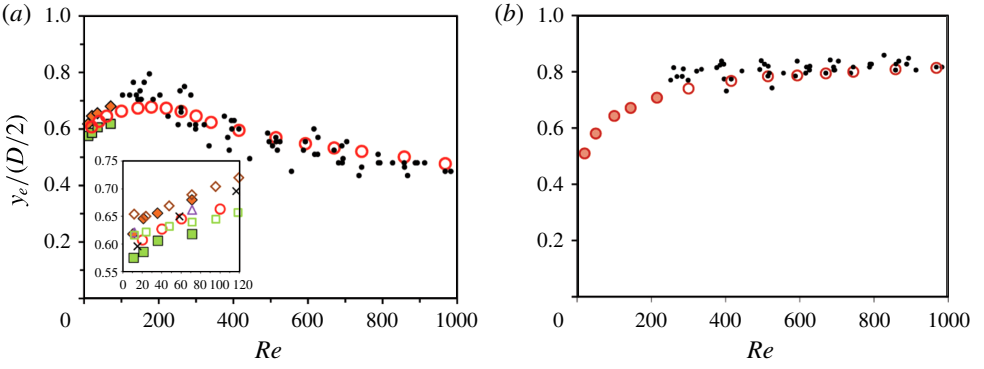

FIGURE 8. (Colour online) Locations of (*a*) the channel face equilibrium positions and (*b*) the channel corner equilibrium positions. The circles represent the results of the present numerical simulations. The experimental results are represented by dots ($d/D = 0.11$) for Miura *et al.* (2014, 2015), filled diamonds ($d/D = 0.083$) and filled squares ($d/D = 0.17$) for Sugihara-Seki (2015), and hollow diamonds ($d/D = 0.075$), hollow triangles ($d/D = 0.12$) and hollow squares ($d/D = 0.16$) for Choi *et al.* (2011), and crosses ($d/D = 0.11$) for Abbas *et al.* (2014). In figure 8(*b*), hollow and filled circles indicate stable and unstable equilibrium positions, respectively.

y_e (Choi *et al.* 2011; Abbas *et al.* 2014; Sugihara-Seki 2015), while larger millimetre scale experiments have shown a decrease in y_e (Miura *et al.* 2014, 2015). These features are well described by the present numerical simulation.

In figure 8(*b*), hollow and filled circles denote stable and unstable channel corner equilibrium positions, respectively. The hollow circles in figure 8(*b*) are in fairly good agreement with the experimental results (Miura *et al.* 2014, 2015), and exhibit a monotonic increase with increasing Re. This monotonic increase in y_e is in agreement with experimental observations of circular tube flows (Segre & Silberberg 1962; Matas *et al.* 2004*a*) and the predictions of perturbation analysis (Asmolov 1999; Matas *et al.* 2009). In circular tube flows, the equilibrium radial position of neutrally buoyant spherical particles, known as the Segre-Silberberg annulus, was reported to move monotonically towards the tube wall with increasing Re up to $Re = 1700$ (Segre & Silberberg 1962; Matas *et al.* 2004*a*). Next, we consider the implication of the results shown in figure 8, in relation to the results of previous studies, mainly theoretical and numerical studies on the inertial migration.

There have been many theoretical studies, based on the perturbation method, investigating the origin of the lateral forces on particles suspended in channel flows. Among them, the effect of curvature in Poiseuille velocity profile was first pointed out by Ho & Leal (1974). From dual perturbation expansions in Re_p and d/D with the condition of $Re_p \ll (d/D)^2$, they indicated for plane Poiseuille flow that the interaction of the stresslet (symmetric force dipole), generated due to the particle rigidity constraint, and its wall correction with the bulk shear flow produces the inward force, whereas the interaction between the stresslet and the curvature of the bulk velocity profile yields the outward force towards the channel wall. Compared with these effects, the lag velocity of the particle and its slip rotation were found to be less important for neutrally buoyant particles. In accord with this conclusion for small particles at low Re_p, the two-dimensional finite element simulations of Feng, Hu & Joseph (1994) indicated that the driving forces of lateral migration for neutrally

buoyant particles consist mainly of the wall repulsion and the lift force caused by the velocity profile curvature even for large particle sizes at relatively large Reynolds numbers. Thus, the equilibrium position of a neutrally buoyant spherical particle in channel flow could be determined by a balance between the outward force due to the shear gradient and the inward force due to the wall effect (Ho & Leal 1974; Matas *et al.* 2004*b*).

For higher Re, Asmolov (1999) extended the matched asymptotic approach of Schonberg & Hinch (1989) up to $Re = 1500$ in the condition of $Re_p \ll 1$ and $d/D \ll 1$, and showed that the equilibrium position in plane Poiseuille flow is shifted progressively towards the channel wall as Re increases. The same trend for Poiseuille flow through circular tubes, which was obtained by Matas *et al.* (2009) based on the matched asympotic expansion, explained successfully the experimental observation of the outward shift of the Segre-Silberberg annulus with Re (Segre & Silberberg 1962; Matas *et al.* 2004*a*). This shift of the equilibrium position was understood by taking the above mentioned two competing lift forces into account; the increase in shear-gradient induced lift force with Re is larger than that in wall-effect induced lift force, so that increasing Re shifts the particle equilibrium positions closer to the tube wall (Asmolov 1999; Matas *et al.* 2004*b*).

With regard to square channel flows, Hood *et al.* (2015) adopted a perturbation method similar to Ho & Leal (1974) and showed that the results of Ho & Leal (1974) hold in a larger parameter space of Re and d/D than the authors assumed. Estimating the stresslet flow field, they concluded that viscous stresses are dominant over the inertial stress even at moderate Reynolds numbers in square channel flows. From the curved velocity profile in the square channel flow, in particular, along the y- (z-) axis and the diagonal in the channel cross-section, the prediction of the outward shift of the equilibrium position with Re may be also applied for the channel face and corner equilibrium positions if the particles are infinitesimally small. This could account for the present results for the channel face equilibrium positions at low Re and the channel corner equilibrium positions (figure 8). However, the channel face equilibrium positions at high Re exhibited the opposite trend. A possible cause may be the finite size ratio $d/D\,(=0.11)$ and consequently the finite particle Reynolds number ($Re_p \approx 2.5$–12.3) in the present numerical study and the experiments (Miura *et al.* 2014, 2015), which violates the assumptions of the matched asymptotic expansion method. According to the study of Hood *et al.* (2015), this result may imply that, due to the finite size effect of the particle, an increase in Re (> 200) increases the lateral force due to the wall effect to a more dominant level than that due to the velocity shear gradient, for a particle placed near the centre of the channel faces. In fact, the present study demonstrates that on the y- (or z-)axis, the lateral forces near the centreline are decreased compared to near the channel wall, as shown in figures 4(*a*)–6(*a*).

The importance of the finite particle size for particle migration properties was pointed out in several studies (Feng *et al.* 1994; Di Carlo 2009; Matas *et al.* 2009; Hood *et al.* 2015). In particular, the experimental study of Matas *et al.* (2004*a*) for circular tube flows reported the presence of a new equilibrium position closer to the tube centre in addition to the Segre–Silberberg annulus at elevated Re, and the majority of the particles were found to lie on the additional inner annulus for $Re > 700$. Since their matched asymptotic expansion analysis for particles of vanishing size did not provide an additional zero of the lateral force, representing a new equilibrium position, in the range of Re from 1 to 2000, they concluded that the presence of the inner annulus observed experimentally is a result of the finite size of the suspended particle (Matas *et al.* 2009).

The shift of the particle positions towards the channel centreline reported in high aspect ratio rectangular microchannel flows (Ciftlik, Ettori & Gijs 2013) may be related to the inward shift of the channel face equilibrium position with high Re (>200). Ciftlik *et al.* (2013) measured fluorescent images of particle streams at downstream positions in the range of Re from 75 to 1500. From their observations in the direction perpendicular to the short channel face, they reported that the positions of the streams are almost constant up to $Re = 300$, and for $300 < Re < 450$ they migrate towards the channel centreline with increasing Re. Figure S3 of their paper showed that, beyond this value, the focusing positions of the particles approach the channel wall as Re increases up to 1500. The inward shift of the particle focusing positions for $300 < Re < 450$ is similar to the present result for the channel face equilibrium position, as shown in figure 8(*a*), although the tendencies in the other ranges of Re are different. These discrepancies may result from differences in experimental conditions, including the aspect ratio of the channel cross-section.

One of the key results of the present study is the large entry length, L_2, for particle focusing. As discussed in the previous section, the first stage of particle migration may be described by considering two competing lateral forces: the outward force due to the shear gradient and the inward force due to the wall effect. Thus, the asymptotic expansion analysis in Re_p and d/D may explain the particle behaviour even at moderate Reynolds numbers in the first stage (Hood *et al.* 2015). However, in the second stage, where the two lateral forces are almost balanced on the heteroclinic orbit, the next order terms of the expansion may be necessary to take into account for describing the migration behaviour precisely. Particle slip velocity as well as slip rotation may play a role in determining the particle lateral motion along the heteroclinic orbit, the contributions of which can be neglected compared to the leading order terms in the first stage. Our results show that at low Re ($< Re_c$), the lateral force acts in the direction from the channel corner equilibrium position to the channel face equilibrium position along all the heteroclinic orbit. This makes the channel face equilibrium position stable and the channel corner equilibrium position unstable. At high Re ($> Re_c$), a saddle point appears on the heteroclinic orbit, and the direction of the lateral force is reversed between the saddle point and the channel corner equilibrium position. This makes the corner equilibrium position stable. It would be important to elucidate the origin of these variations of the lateral force in the second stage of particle migration, since this will enable us to estimate the entry length, L_2, for the particle focusing.

Another important issue we need to explore in the near future is the effect of the hydrodynamic interaction between particles, since it may affect the location and the number of equilibrium positions (Humphry *et al.* 2010) and be a possible cause for the dispersion of particles observed experimentally (Di Carlo 2009; Abbas *et al.* 2014). In addition, Abbas *et al.* (2014) found that particles suspended in square channel flows are preferentially located near the channel centre at $Re < 1$, opposed to predictions based on the Stokes flow or extrapolation from inertial migration at higher Re, and this phenomenon was considered to be generated by the shear-induced particle interactions. It may be that the inter-particle interaction affects also the migration behaviour at higher Re. The effect of particle size relative to the channel width is also important, considering the difference in Reynolds number and particle Reynolds number. This effect has been investigated by a regular perturbation analysis of the Stokes equation (Hood *et al.* 2015). A recent experimental study in our laboratory for $100 \leqslant Re \leqslant 1000$ has demonstrated considerably enhanced focusing properties for larger particles near the equilibrium positions, whereas a clear dependence on

particle size has not been observed for the locations of the equilibrium position and the transition behaviours in the range of $0.05 \leqslant d/D \leqslant 0.11$ (Miura *et al.* 2015). The significant effect on the particle focusing may reflect the high power dependence of the magnitude of the lateral forces on the size ratio. Further detailed experimental and numerical studies are necessary to elucidate this effect. Another issue to explore is related to the physics near $Re = Re_c$. At $Re \approx Re_c$, we have revealed extremely small lateral forces along the heteroclinic orbit and the presence of a new equilibrium position on the orbit. It is uncertain whether the saddle point and the new equilibrium point appear simultaneously and whether other equilibrium positions are present on the heteroclinic orbit. It would be interesting to carry further investigations on these issues.

4. Conclusions

We have performed numerical simulations of the motion of a spherical particle suspended in square channel flows, at a size ratio of particle diameter to channel width of 0.11, in the range of Re from 20 to 1000. The obtained results describe well the experimental observations of particle distributions in dilute suspension flows through micro and millimetre scale channels, and elucidate the migration behaviours of particles approaching the equilibrium positions in the channel cross-section as they travel downstream.

Acknowledgements

This research was partially supported by JSPS KAKENHI grant 25630057 and by the ORDIST group fund at Kansai University. We thank Drs T. Kajishima and S. Takeuchi, Osaka University, for providing valuable information regarding the numerical simulation method, and Dr E. Watters for English proofreading.

REFERENCES

ABBAS, M., MAGAUD, P., GAO, Y. & GEOFFROY, S. 2014 Migration of finite sized particles in a laminar square channel flow from low to high Reynolds numbers. *Phys. Fluids* **26**, 123301.

ASMOLOV, E. S. 1999 The inertial lift on a spherical particle in a plane Poiseuille flow at large channel Reynolds number. *J. Fluid Mech.* **381**, 63–87.

BHAGAT, A. A. S., KUNTAEGOWDANAHALLI, S. S. & PAPAUTSKY, I. 2008 Enhanced particle filtration in straight microchannels using shear-modulated inertial migration. *Phys. Fluids* **20**, 101702.

BIRD, R. B., STEWART, W. & LIGHTFOOT, E. 2007 *Transport Phenomena*, 2nd edn. p. 187. Wiley.

CHOI, Y., SEO, K. & LEE, S. 2011 Lateral and cross-lateral focusing of spherical particles in a square microchannel. *Lab on a Chip* **11**, 460–465.

CHUN, B. & LADD, A. J. C. 2006 Inertial migration of neutrally buoyant particles in a square duct: an investigation of multiple equilibrium positions. *Phys. Fluids* **18**, 031704.

CIFTLICK, A. T., ETTORI, M. & GIJS, M. A. M. 2013 High throughput-per-footprint inertial focusing. *Small* **9**, 2764–2773.

DI CARLO, D. 2009 Inertial microfluidics. *Lab on a Chip* **9**, 3038–3046.

DI CARLO, D., EDD, J. F., HUMPHRY, K. J., STONE, A. H. & TONER, M. 2009 Particle segregation and dynamics in confined flows. *Phys. Rev. Lett.* **102**, 094503.

DI CARLO, D., IRIMA, D., TOMPKINS, R. G. & TONER, M. 2007 Continuous inertial focusing, ordering, and separation of particles in microchannels. *Proc. Natl Acad. Sci. USA* **104**, 18892–18897.

FENG, J., HU, H. H. & JOSEPH, D. D. 1994 Direct simulation of initial value problems for the motion of solid bodies in a newtonian fluid. Part 2. Couette flow and Poiseuille flow. *J. Fluid Mech.* **277**, 271–301.

HO, B. P. & LEAL, L. G. 1974 Inertial migration of rigid spheres in two-dimensional unidirectional flow. *J. Fluid Mech.* **65**, 365–400.

HOOD, K., LEE, S. & ROPER, M. 2015 Inertial migration of a rigid sphere in three-dimensional Poiseuille flow. *J. Fluid Mech.* **765**, 452–479.

HUMPHRY, K. J., KULKAMI, P. M., WEITZ, D. A., MORRIS, J. F. & STONE, H. A. 2010 Axial and lateral particle ordering in finite Reynolds number channel flows. *Phys. Fluids* **22**, 081703.

KAJISHIMA, T., TAKIGUCHI, S., HAMASAKI, H. & MIYAKE, Y. 2001 Turbulence structure of particle-laden flow in a vertical plane channel due to vortex shedding. *JSME J.* B **44**, 526–535.

KIM, Y. W. & YOO, J. Y. 2008 The lateral migration of neutrally-buoyant spheres transported through square microchannels. *J. Micromech. Microengng* **18**, 065015.

MATAS, J.-P., MORRIS, J. F. & GUAZZELLI, E. 2004*a* Inertial migration of rigid spherical particles in Poiseuille flow. *J. Fluid Mech.* **515**, 171–195.

MATAS, J.-P., MORRIS, J. F. & GUAZZELLI, E. 2004*b* Lateral forces on a sphere. *Oil Gas Sci. Tech. Rev. JFP* **59**, 59–70.

MATAS, J.-P., MORRIS, J. F. & GUAZZELLI, E. 2009 Lateral force on a rigid sphere in large-inertia laminar pipe flow. *J. Fluid Mech.* **621**, 59–67.

MIURA, K., HARADA, S., ITANO, T. & SUGIHARA-SEKI, M. 2015 Inertial migration of spheres in square channel flows. *Kyoto University RIMS Kokyuroku* **1940**, 68–75 (in Japanese).

MIURA, K., ITANO, T. & SUGIHARA-SEKI, M. 2014 Inertial migration of neutrally buoyant spheres in a pressure-driven flow through square channels. *J. Fluid Mech.* **749**, 320–330.

NAKAGAWA, N., MIURA, K., OTAMO, R., MAKINO, M. & SUGIHARA-SEKI, M. 2014 Lateral migration of a spherical particle in channel flow. WCCM XI, ECCM V, ECFD VI. MS007C.

NAKAYAMA, Y. & YAMAMOTO, R. 2005 Simulation method to resolve hydrodynamic interactions in colloidal dispersions. *Phys. Rev.* E **71**, 036707.

SCHONBERG, J. A. & HINCH, E. J. 1989 Inertial migration of a sphere in Poiseuille flow. *J. Fluid Mech.* **203**, 517–524.

SEGRE, G. & SILBERBERG, A. 1961 Radial particle displacements in Poiseuille flow of suspensions. *Nature* **189**, 209–210.

SEGRE, G. & SILBERBERG, A. 1962 Behaviour of macroscopic rigid spheres in Poiseuille flow. Part 2. Experimental results and interpretation. *J. Fluid Mech.* **14**, 136–157.

SUGIHARA-SEKI, M. 2015 Inertial migration of spherical particles in channel flows. *Nagare* **34** (in press).